# Evolution of Flare Rates in GKM Stars Younger than 300 Myr

Adina D. Feinstein[1, *] and Darryl Z. Seligman [2, †]

[1] *Laboratory for Atmospheric and Space Physics, University of Colorado Boulder, UCB 600, Boulder, CO 80309*
[2] *Department of Astronomy and Carl Sagan Institute, Cornell University, 122 Sciences Drive, Ithaca, NY 14853*

## ABSTRACT

Stellar flares are short-duration ($<$ hours) bursts of radiation associated with surface magnetic reconnection events. Stellar magnetic activity generally decreases as a function of both age and of Rossby number, $R_0$, a measure of the relative dominance of the convective and rotational dynamos. For those reasons, it is worthwhile analyzing the flare population level characteristics for young, rapidly rotating stars. With this motivation, we select a sample of stars that are either (i) members, (ii) candidate members or (iii) high-probability of being members of 26 nearby young moving groups, clusters, or associations all known to be less than 300 Myr old that have been observed by the Transiting Exoplanet Survey Satellite (TESS) at 2-minute cadence. With this sample of $\sim$ n stars younger than 300 Myr, we present detections and characterizations of the flare properties. We identified n flares originating from n stars. Moreover, we robustly measured the rotation periods of $1,847$ stars. Finally, we measure the flare frequency distribution (FFD) slope as a function of both age and spectral type. We find the FFD slope, $\alpha$, saturates for all spectral types at $\alpha = -0.5$ and does not evolve over 300 Myr. Additionally, we find that $R_0$ and flare rate for stars $t_{\rm age} = 100 - 300$ Myr are saturated out to $R_0 = 0.12$, which is consistent with other indicators of magnetic activity. We find the FFD slope for stars with $R_0 \leq 0.14$ are shallower than stars with $R_0 > 0.14$, suggesting the Coriolis force plays a role in generating more high-energy flares. We cross match our targets with *GALEX* and find no correlation between flare rate and Far- and Near-Ultraviolet flux. Finally, we compare the flare rates of planet hosting stars to comparable, larger samples of stars and find the majority of these stars are relatively flare quiet. This may impact the atmospheric evolution of young short-period exoplanets.

## 1. INTRODUCTION

Stellar flares are the radiation component of magnetic reconnection events (). Such events are readily seen on the Sun (), particularly now as we enter a maximum in the solar cycle (). Such events can be used to understand the magnetic activity of other stars (). Additionally, by studying stellar flares we can understand how these short-duration events may impact short-period exoplanet evolution (). While we cannot resolve stellar flare events on other stars, we can detect and characterize both spectroscopic and photometric signatures of such events. Spectroscopic characterization of stellar flares inform our understanding of non-thermal processes affiliated with such events, e.g. coronal mass ejections () or proton beams (). They can also inform our understanding of stellar plasma is displaced during these events ().

Photometric observations of stars are more readily available thanks to exoplanet missions, and allow us to statistically characterize flare rates and energies. Within time-series photometry, stellar flares can be identified by a sharp rise in the stellar flux and a subsequent exponential decay, corresponding to the cooling rate (). *Kepler* provided long-baseline high-cadence observations used to identify stellar flares. There has been extensive studies of flares in *Kepler* data, from the statistics of superflares on solar-type stars (Notsu et al. 2013; Shibayama et al. 2013; Maehara et al. 2015; Okamoto et al. 2021, e.g.) to low-mass stars (Hawley et al. 2014; Silverberg et al. 2016, e.g.). Davenport et al. (2019) found that flare activity decreased with increasing rotation period for 347 GKM stars. However, the flare frequency distribution (FFD) slope did not change significantly as a function of age. As a caveat, the ages of the stars were determined based on their rotation periods alone, relying on the assumption that gyrochronology alone accurately ages stars.

After the failure of two reaction wheels, *Kepler* was repurposed to the *K2* mission (Howell et al. 2014). *K2*

---

provided 70-day baseline observations for a handful of young stars in groups such as Upper Scorpius, Pleiades, Hyades, and Praespe clusters. Ilin et al. (2019) analyzed flares K and M stars in these clusters and measured FFD slopes of ...

More recently, the Transiting Exoplanet Survey Satellite (TESS; Ricker et al. 2015) has provided near all-sky photometric observations at 30-minute cadence or less. Such an observing strategy has allowed for more detailed studies of young stellar flares from nearby young moving groups and associations, which are disperse in the sky ().

The paper is presented as follows. In Section 2, we describe our sample, stellar flare identification and fitting methods, and methods for measuring stellar rotation periods. In Section 3, we present our flare-frequency distribution (FFD) fits as a function of stellar age, $T_{\mathrm{eff}}$, and $R_0$. In Section 4, we search for correlations in flare rates with FUV and NUV observations from *GALEX* and place the flare rates of young planet hosting stars in the context of our broader sample. We conclude in Section 5. We provide additional figures and tables in Section A.

## 2. TESS LIGHT CURVE CHARACTERIZATION

In this section, we provide an overview of the methodology associated with this paper. The various methods described here are pertinent to the remainder of the paper. Specifically, we describe the sample selection in subsection 2.1, TESS light curve analysis in 2.2, flare identification in subsection 2.3, flare models in 2.4, flare quality checks in 2.5, and measurement of stellar rotaiton periods in 2.6.

### 2.1. *Sample Selection*

In this paper, we select a sample of stars that have $< 300$ Myr ages based on their affiliation with nearby young moving group, clusters and associations. This provides an independant constraint on the age, which is more robust than only using the rotational periods. Moreover, we select stars that have been observed with TESS with 2-minute cadence. With these criteria, we obtain light curves for a sample of 3,163 young stars in total.

With these stars selected, we then run the convolutional neural network, `stella`, on each light curve to identify stellar flares (Feinstein et al. 2020a). In order to model the flare profile, we employ the analytical model developed by Tovar Mendoza et al. (2022). This model is able to simultaneously (i) fit the flares and (ii) measure the equivalent duration and energy associated with each flare.

A primary goal of this paper is to measure the evolution of the stellar flare rate and its dependance on the stellar age. Particularly, we are interested in this dependancy for stars with ages $1 \leq t_{\mathrm{age}} \leq 250\,\mathrm{Myr}$. To this end, we used the MOCA Data Base (Gagné et al. in prep.) to identify nearby young moving groups, associations, and open clusters with known ages which satisfied our criteria. From this database we identified 26 unique groups from which we created our sample of stars. The final selected targets were required to be: (i) confirmed members, (ii) high-likelihood candidate members, or (iii) candidate members. These rather stringent cuts resulted in a catalog of 30,889 stars across 26 associations. We summarize the sample and ages for each association (and therefore star) in Table 1.

**Table 1.** Adopted Ages of each Young Stellar Population and Number of Stars per Group

| Population | Age [Myr] | $N_{\mathrm{stars}}$ | Ref. |
|---|---|---|---|
| AB Doradus | $133^{+15}_{-20}$ | 88 | 1 |
| Blanco 1 | $137.1^{+7.0}_{-33}$ | 428 | 2 |
| Carina | 45 | 94 | 3 |
| Carina-Musca | 32 | 35 | 4 |
| Chamaeleon | 5 | 424 | 5 |
| Columba | 42 | 126 | 3 |
| Greater Taurus Subgroup 5 | 8.5 | 56 | 4 |
| Greater Taurus Subgroup 8 | 4.5 | 122 | 4 |
| Lower Centaurus Crux | 15 | 761 | 6 |
| MELANGE-1 | $250^{+50}_{-70}$ | 19 | 7 |
| Octans | $35\pm5$ | 64 | 8 |
| Pisces Eridanis | 120 | 219 | 9 |
| Pleiades | $127.4^{+6.3}_{-10}$ | 1421 | 2 |
| $\alpha$ Persei | $79^{+1.5}_{-2.3}$ | 625 | 2 |
| IC 2602 system | $52.5^{+2.2}_{-3.7}$ | 160 | 2 |
| NGC 2451A | 48.5 | 59 | 4 |
| Oh 59 | 162.2 | 62 | 10 |
| Platais 9 | 50 | 124 | 11 |
| RSG2 | 126 | 145 | 12 |
| Theia 301 | 195 | 437 | 10 |
| Theia 95 | 30.2 | 230 | 10 |
| TW Hydrae | 10 | 24 | 3 |
| Upper Centaurus Lupus | $16\pm2$ | 696 | 6 |
| Upper Scorpius | 10 | 106 | 6 |
| Vela-CG4 | 33.7 | 299 | 4 |
| Total | | 6,824 | |

NOTE—Age references: (1) Gagné et al. (2018); (2) Galindo-Guil et al. (2022); (3) Bell et al. (2015); (4) Kerr et al. (2021); (5) Luhman (2007); (6) Pecaut & Mamajek (2016); (7) Tofflemire et al. (2021); (8) Murphy & Lawson (2015); (9) Curtis et al. (2019); (10) Kounkel et al. (2020); (11) Tarricq et al. (2021); (12) Röser et al. (2016)

## 2.2. *TESS Light Curves*

As described in the previous subsection, we only select stars in our sample for which TESS light curves have been obtained with 2-minute cadance. The reason for doing this is so that we are able to resolve and accure accurately measure the energies of flares for each of these stars (Howard & MacGregor 2022). We crossmatched our sample with the TESS Input Catalog (TIC) based on their RA and Dec. In order for a star to be considered as a member of the catalog, , we required that the distance between the target and the nearest TIC was within < 1".

This process provided a final sample of 5,725 unique targets. These targets have each been observed at a 2-minute cadence between TESS Sector 1 and Sector 67. These are the latest available sectors at the time that this analysis was performed. In Figure 1, we show the distribution of the on sky positions of the final sample. It is evident that many targets exhibit strong tendency for proximitry towards the northern and southern ecliptic poles (Figure 1). Therefore, many of these targets were observed over multiple sectors all of which observed the ecliptic poles. The entirety of the available data yielded a total of 17,964 light curves, an average of $\sim 3$ light curves per target (although with significant spread across targets).

## 2.3. *Flare Identification*

Once we had the lightcurves for each target, we performed the following procedur to identify stellar flares. First, we implemented the machine learning flare-identification methods presented and described in Feinstein et al. (2020b). This method relies on the fact that all flare events have similar time-dependent morphologies. These flare-profiles can generally be described as a sharp rise followed by an exponential decay in the white light curve. The identification-technique implements a convolutional neural network (CNN), `stella` (Feinstein et al. 2020b). The neural network was trained to identify flare events in TESS 2-minute data using a catalogue of flare events from TESS Sectors 1 and 2 that were validated by-eye (Günther et al. 2020).

There are many benefits to using the CNN for stellar flare identification. Primarily, the CNN is advantageous because it is insensitive to the stellar baseline flux. This feature inherently stems from the fact that the network is trained to search *only* based on flare morphology. It is therefore relatively insensitive to the absolute flux levels, so long as the inherent noise does not overwhelm the signal itself. One advantage of this is that rotational modulation peaks — which are themselves driven
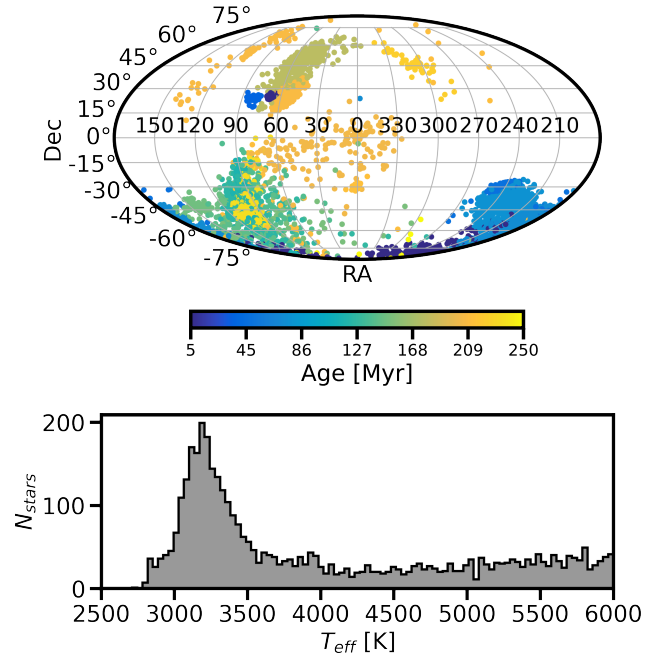


**Figure 1.** Top: Distribution of our selected sample across the sky and colored by the adopted age of the association (see Table 1). The all-sky coverage by TESS has unlocked new populations of stars to observe. We take advantage of this observing strategy to measure flare rates across 26 different nearby young moving groups, clusters, and associations. Bottom: Distribution of adopted effective temperatures, $T_{\rm eff}$ [K] for stars in our sample. We include all stars with $T_{\rm eff} \leq 6000\,{\rm K}$.

by stellar heterogeneities — are not accidentally identified as flares. This is especially advantageous for our sample of young stars, which readily exhibit rotational modulatioin and associated peaks in their light curves.

Based on these advantages, the final compiled sample of flares is *unbiased* towards low-amplitude/low-energy flares. It is important to note that these low-energy events are typically not identified in traditional sigma-outlier identification methods (Chang et al. 2015).

The `stella` CNN models calculates the probability that a data point in a light curve is associated with a flaring event. Specifically, it taakes the light curve (time, flux, flux error) as an input and returns an array with values of [0,1], which are treated as the probability a data point is (1) or is not (0) part of a flare. We ran every light curve through 10 independant `stella` models to ensure that our statistics were accurate. We then averaged the output probabilities for each 10 model runs to be the final prediction per observation.

In order to identify a single flare event, the `stella` code uses the predictions per data point to group together points. We modified this stage of identification slightly from the original flare-identification method.

4

Specifically, we identified all data points with a probability of being associated with a flare of $P > 0.75$. Any data points that were within 4 cadences of each other were considered to be a single flare event. We did not consider any potential flares that had three or fewer points with $P > 0.75$. This was motivated by the fact that sometimes a single-point outlier is assigned a high probability of being a flare. Therefore, we simply neglected these events. We assigned the probability of the whole flare event as the probability of the peak data point.
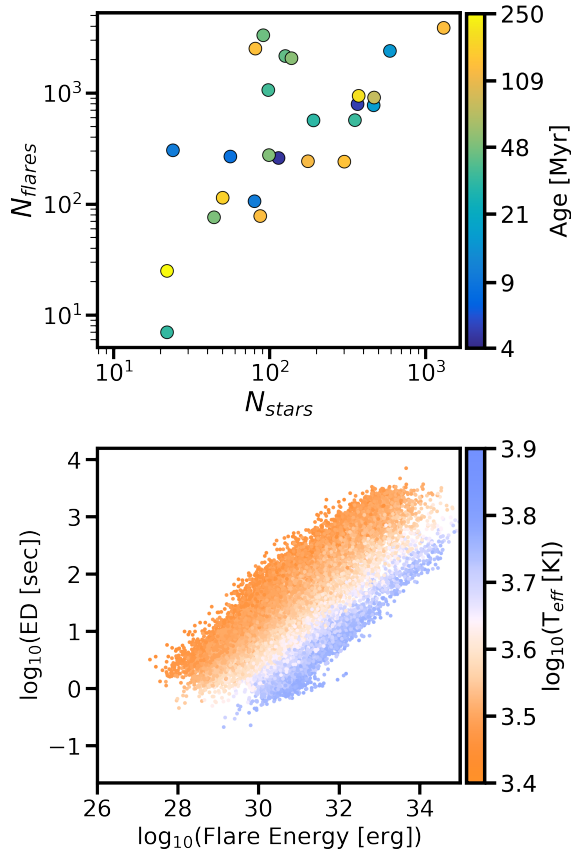


**Figure 2.** High level summary of the demographics of flares in our sample. Top: The number of flares identified compared to the number of stars in each nearby young moving group, cluster, or association. A one-to-one relationship is expected. Middle: The distribution measured TESS energies and equivalent durations of flares in our sample, colored by the probability of the flare as identified with `stella`. Bottom: Same as the middle plot, except colored by the $T_{\rm eff}$ [K] of the star. We limit our sample to stars with $T_{\rm eff} \leq 6000\,$K.

### 2.4. *Modeling Flare Properties*

As described in the previous subsection, flares are well-described in light curves as a sudden increase in flux followed by an exponential decay. For this paper,

we used the analytical flare model,Llamaradas Estelares which was presented in Tovar Mendoza et al. (2022)[1]. We used these models to fit the flares and extract the flare parameters in all of the light curves of our sample. This model builds upon the model presented in Davenport et al. (2014). Specifically, it includes the convolution of a Gaussian with a double exponential model in the flare profile.

The analytical model is robust in that it is able to accounts for multiple inherent features of flares. Specifically, it can incorporate the flare (i) amplitude, (ii) heating timescale, (iii) rapid cooling phase timescale, and (iv) slow cooling phase timescale . We implemented a nonlinear least squares optimization to fit for the time of the flare peak ($t_{\rm peak}$), full width at half maximum (FWHM), and the amplitude ($A$) of each flare in the sample. We combine the model with a second-order polynomial fit to a 1.2-hour baseline before and after the flare during only the fitting stage. This was implemented in order to account for any rotational modulation, and therefore was particularly relevant for the rapid rotators.

We calculated the equivalent duration, ED, of the flare by performing a numerical integration of the flare flux with respect to time. We calculate the flare energy, $E_{\rm flare}$, using,

$$E_{\rm flare} = L_\star\, A\, {\rm ED}\, s\,. \qquad (1)$$

In equation 1, $L_\star$ is the luminosity of the star and $s$ is a scaling factor defined as $s = B_\lambda(T_{\rm eff})/B_\lambda(T_{\rm flare})$, where $B_\lambda(T)$ is the Planck function. We assume that the flare temperature is 9000 K ().

### 2.5. *Flare Quality Checks*

In this subsection, we describe the methodology we employ to ensure that flares identified by the CNN are high quality. The `stella` CNNs were trained on data from TESS Sectors 1 and 2. However, the noise properties are variable aross sectors in TESS data. The CNNs are therefore unable to accurately account for and capture this variation when operating on different sectors. Moreover, the original CNNs were only trained on a sample of 1,228 stars. This sample does not necessarily encapsulate all or even a sufficient distribution of variable stars types, such as eclipsing binaries, RR Lyraes, and fast rotators with rotation periods $P_{\rm rot} < 1$ day. We therefore apply additional quality checks to ensure our flare sample has little to no contamination from other sources.

[1] https://github.com/lupitatovar/Llamaradas-Estelares

Specifically, we remove flares from our sample which did not satisfy one or more of the following criteria.

1. The amplitude of the flare must be $> 0.01$, or 1%. This follows the limits set by Feinstein et al. (2020b).

2. The flare amplitude must be at least twice the standard deviation of the light curve 30 minutes before and 45 minutes after the flare. This ensures that the feature is not a sharp noise artifact.

3. The fitted flare model parameters must be physically motivated: FWHM $> 0$; $A > 0$; ED $> 0$.

4. The flare parameters must be $\sigma_A < 0.5$ and $\sigma_{t_{\mathrm{peak}}} < 0.01$.

We find that when the errors on the first criteria are larger than the cut-offs, the flares are often simply mischaracterized noise.

As a final check, we performed an exhaustive by-eye verification of flares from light curves for stars with flare rates, $\mathscr{R} > 1\,\mathrm{day}^{-1}$. These stars generally tend to have $T_{\mathrm{eff}} > 5000\,\mathrm{K}$ and TESS magnitudes $< 8$. Therefore, their light curves are dominated by sharp noise which `stella` often mischaracterizes as flares.

As a final cut, the sample only includes events that have a probability $P \geq 90\%$ of being a true flare. After performing these additional checks, we obtain a final flare sample of n flares originating from n stars (Figure 2). n% of the flares have probabilities of $P \geq 90\%$ of being true; n% of the flares have probabilities of $P \geq 99\%$ of being true.

### 2.6. *Measuring Rotation Periods*

In this paper we have two primary goals. The first is to improve our understanding of flare statistics across ages for young stars. Seligman et al. (2022) demonstrated that stars with low Rossby numbers $R_0 < 0.13$ exhibit shallower flare frequency distribution slopes. These shallower slopes are caused by an excess of high energy flares compared to lower energy flares originating from these sources. In addition to improving flare statistics, we aim to expand the sample for which flare frequency slope and rossby number (from $P_{\mathrm{rot}}$) have been measured.

In order to perform this, we describe how we measure stellar rotation periods from the TESS light curves. To this end we used `michael`[2] which is an open-source Python package that robustly measures $P_{\mathrm{rot}}$ using

a combination traditional Lomb-Scargle periodograms and wavelet transformations (Hall et al. submitted). `michael` measures $P_{\mathrm{rot}}$ using the `eleanor` package, which extracts light curves from the TESS Full-Frame Images (FFIs; Feinstein et al. 2019).

We ran `michael` on all stars in our samples from which flares were identified. The estimated rotational periods were subsequently vetted by-eye with the `michael` diagnostic plots. This vetting was implemented to ensure that the measured $P_{\mathrm{rot}}$ was not a harmonic of the true $P_{\mathrm{rot}}$. In total, we robustly measured rotation periods for 1,847 stars.

### 3. RESULTS

We analyze our new flare sample from three perspectives. First, we perform the standard FFD fitting of a power-law to the distribution of flare energies. Second, we fit the FFD with the prescription in Gershberg (1972), which fits for both the FFD slope and y-intercept. Third, we fit a truncated power-las to the distribution of flare amplitudes, to determine if there is a correlation between $R_0$ and flare distributions.

The number of stars, and consequently flares, per each association varied greatly, due to the limited number of stars observed at TESS 2-minute cadence. Therefore, instead of measuring FFD properties as a function of association, we opted to group stars by effective temperature, $T_{\mathrm{eff}}$, and average adopted association age. We grouped stars in the following $T_{\mathrm{eff}}$ space: M-stars below the fully convective boundary ($T_{\mathrm{eff}} = 2300 - 3400\,\mathrm{K}$), early type M-stars ($T_{\mathrm{eff}} = 3400 - 3850\,\mathrm{K}$), late K-stars ($T_{\mathrm{eff}} = 3850 - 4440\,\mathrm{K}$), early K-stars ($T_{\mathrm{eff}} = 4440 - 5270\,\mathrm{K}$), and G-stars ($T_{\mathrm{eff}} = 5270 - 5930\,\mathrm{K}$). We did not include any stars hotter than $T_{\mathrm{eff}} > 5930\,\mathrm{K}$, as these stars are dominated by noise in the TESS observations. Additionally, we grouped stars in the following age space: $4 - 10\,\mathrm{Myr}$, $10 - 20\,\mathrm{Myr}$, $20 - 40\,\mathrm{Myr}$, $40 - 50\,\mathrm{Myr}$, $70 - 80\,\mathrm{Myr}$, $120 - 150\,\mathrm{Myr}$, and $150 - 300\,\mathrm{Myr}$. We note that there is a gap in age from $50 - 70\,\mathrm{Myr}$, which could be expanded with the identification of more associations in this age range. However, for the purposes of this work, we do not include additional sources which may fall in this age range.

### 3.1. *Standard Power-Law Fits*

From the $T_{\mathrm{eff}}$ and age bins described above, we binned the flares in each subgroup and fit their FFD slopes, approximated as a power-law. Flares were binned into 25 bins in log-space from $10^{27} - 10^{35}\,\mathrm{erg}$. We fit the FFDs from the energy bin with the maximum flare rate and energies higher than that. We opt to do this as bins of lower energies may be incomplete, and the turnover in the FFD cannot be accurately modeled as a power-law.

We fit the FFD using the MCMC method implemented in `emcee` (Goodman & Weare 2010; Foreman-Mackey et al. 2013) and fit for the slope, $\alpha$, y-intercept, $b$, and an additional noise term, $f$, which accounts for an underestimation of the errors on each bin. We initialized the MCMC fit with 300 walkers and ran our fit over 5000 steps. Upon visual inspection, we discarded the first 100 steps; onwards the steps were fully burned-in. The full FFDs are presented in Figure A1, along with 100 samples from the MCMC fit. The measured FFD slopes, $\alpha$ are presented in Figure 3. We approximate the error on the slope as the lower 16$^{\text{th}}$ and upper 84$^{\text{th}}$ percentiles from the MCMC fit.

There is a $3\sigma$ discrepancy between the FFD slope measured in Ilin et al. (2021) and the work presented here at ages $\sim 120\,\text{Myr}$. This discrepancy could be the result of several factors. First, Ilin et al. (2021) used the *K2* 30-minute light curves. This would result in a sample biased towards the highest-energy flares which could be sampled at this cadence. Our flare detection method is less-biased towards the low-energy flares due to the 2-minute cadence from TESS and our flare detection algorithm. Second, our sample has $\sim 2\times$ the number of stars and $\sim 7\times$ the number of flares than their sample. This could result in a more complete FFD compared to previous work.

### 3.2. *Truncated Power-Law Fits*

We follow the prescription presented in Seligman et al. (2022). Namely, we fit a truncated power-law distribution of the form

$$dp/dA \propto A^{-\alpha_T} e^{-A/A_*} \qquad (2)$$

where $A$ is the amplitude of the flare, $A_*$ is a flare amplitude cutoff parameter and $\alpha_T$ is the slope, rather than $\alpha$. We fit the slopes using the MCMC method implemented in `emcee` (Goodman & Weare 2010; Foreman-Mackey et al. 2013), using the log-likelihood function in Seligman et al. (2022). We fit for $A_*$ and $\alpha_T$. We initialized the MCMC fit with textcolorredn walkers and evaluated the fit over textcolorredn steps. The first textcolorredn steps were discarded upon visual inspection. The results are presented in Figure 4.

### 3.3. *Flare Rates Compared to $R_0$*

The Rossby number, $R_0$, is a term which marginalizes over several properties which are known to affect the stellar dynamo, such as the rotation period and stellar mass. We convert our measured rotation periods to $R_0$, which is defined as $R_0 = P_{\text{rot}}/\tau$, where $\tau$ is the convective turnover time. We approximate $\tau$ following the

prescription in Wright et al. (2011). We equate the flare rates for individual stars as

$$\mathscr{R} = \frac{1}{t_{\text{obs}}} \left( \sum_{i=1}^{N} p_i \right) \qquad (3)$$

where $\mathscr{R}$ is the flare rate in units of day$^{-1}$, $t_{\text{obs}}$ is the total amount of time a target was observed with TESS, and $p_i$ is the probability that flare $i$ is a true flare as assigned by `stella`. We compare the calculated $R_0$ to measured flare rates for all stars we measured $P_{\text{rot}}$ for. The results are presented in Figure 5.

We evaluate the relationship between age, spectral type, flare rate, and $R_0$. We divide the sample between stars younger and older than 50 Myr, which roughly correlates to the age at which GKM stars turn onto the main sequence. For stars younger than 50 Myr, we find the flare rate slightly decreases with increasing $R_0$, although there is a significant amount of scatter in this relationship. For stars between $50 - 250$ Myr, we see this relationship much clearer. For M stars, we see minimal evolution in both average flare rate and $R_0$ between the two samples. For K stars, we see $R_0$ evolving over the first 250 Myr, while the scatter in the flare rate decreases. For G stars, we see the scatter in $R_0$ decreasing, and the average flare rate across the sample decreases. We present a compiled histogram for all stars in our sample in the right column of Figure 5.

To better understand this trend, we fit three types of functions: (i) a constant value, (ii) a single power law, and (iii) a piece-wise function consisting of a constant value and a power law. For (iii), we computed these fits across a range of $R_0$ for where the turnover should occur. We binned the cumulative dataset consisting of all GKM stars into 50 evenly-spaced bins in log-space from $log_{10}(R_0) = [-2, 0]$. We computed the $\chi^2$ between each of these fits and the data. For stars $4.5 - 50$ Myr, we find the distribution is best-fit with a single power law with slope $m = -0.243 \pm 0.043$ and y-intercept $b = -1.221 \pm 0.061$. Converting the $\chi^2$ to a standard deviation, we find a single fit is preferred by $\sim 3\sigma$. For stars $50 - 250$ Myr, we find the distribution is best-fit with a piece-wise function of the form

$$\mathscr{R} = \begin{cases} C & R_0 \leq 0.15 \\ 10^b * R_0^m & R_0 > 0.15 \end{cases} \qquad (4)$$

where $\mathscr{R}$ is the flare rate, $C = 0.126 \pm 0.006$, $m = -0.986 \pm 0.119$, and $b = -1.687 \pm 0.078$. We test how our bin size affected our $R_0$ turnover. To do this, we refit our data assuming binning from $20 - 100$ bins and find $R_0$ to be consistent with $R_0 = 0.15 \pm 0.02$. The location of the turnover is consistent to within $1\sigma$ with
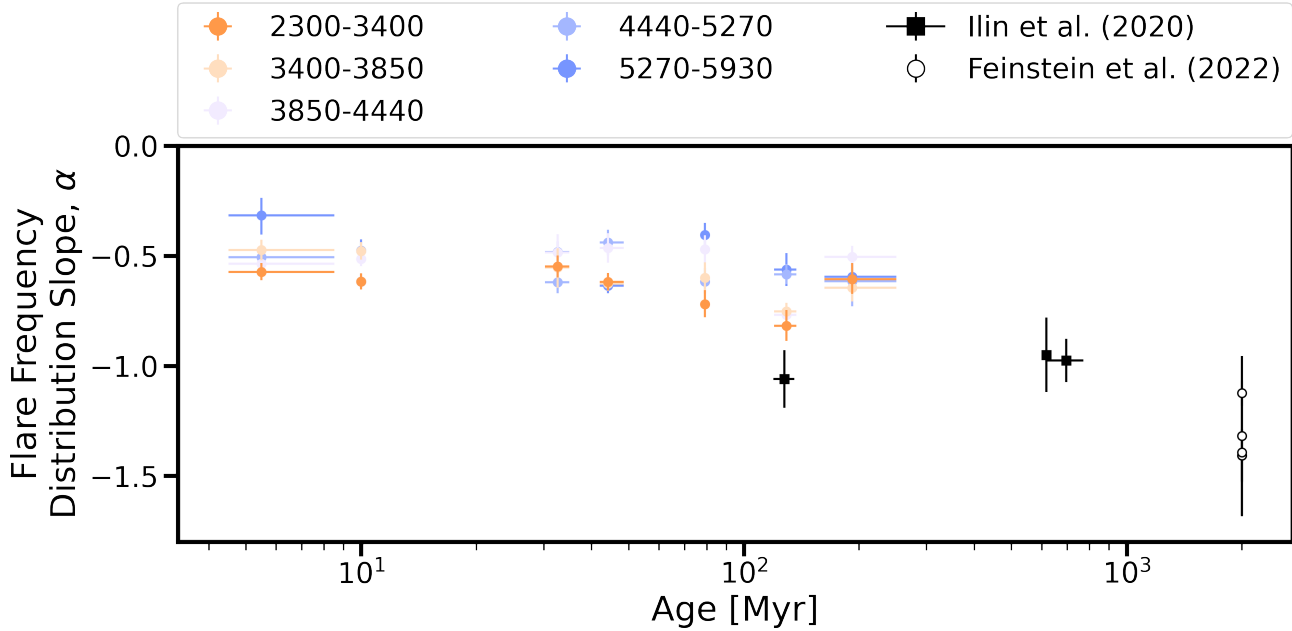
**Figure 3.** Measured flare-frequency distribution slopes, $\alpha$, as a function of stellar effective temperature, $T_{\rm eff}$ and age.
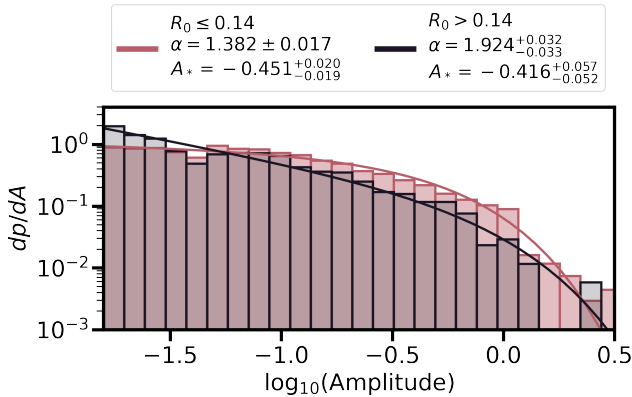


**Figure 4.** Flare frequency distributions, as a function of flare amplitude, for stars with $R_0 \leq 0.12$ (red) and stars with $R_0 > 0.12$ (black). We present the best-fit model, and the best-fit values of the model slope and normalization factor in the legends. Our sample of $R_0 \leq 0.12$ includes 13,132 flares from 800 stars; our sample of $R_0 > 0.12$ includes 5,603 flares from 747 stars. We find the stars with smaller Rossby numbers have shallower slopes, consistent with more, high-energy flares and potentially larger convective regions (Seligman et al. 2022).

what has been seen in other observations of magnetic saturation for partially and fully convective stars (e.g. $L_X/L_{\rm bol}$; Wright et al. 2018).

## 4. DISCUSSION

### 4.1. *Correlations with Far- and Near-Ultraviolet Flux*

X-ray luminosity surveys of stars have revealed a saturation limit with respect to the star's rotation period.

Namely, there is no evolution in $L_X/L_{\rm bol}$ for stars with $P_{\rm rot} < 10$ days (Pizzolato et al. 2003).

The Far- and Near-Ultraviolet (FUV/NUV) is another tracer of magnetic activity. Young stars are known to have excess luminosity in both of these wavelengths (). We use archival observations from the *Galaxy Evolution Explorer* (*GALEX*; Martin et al. 2005) to search for trends in FUV/NUV saturation and flare rate saturation. *GALEX* provides broad FUV photometry from $1350-1750$Å and NUV photometry from $1750-2750$Å. We crossmatch our targets with the *GALEX* catalog. We follow the sample selection methods outline in (Schneider & Shkolnik 2018). We search a $10''$ radius around the coordinates of each target in our sample. We include targets with no bad photometric flags (e.g. `fuv_artifact` or `nuv_artifact == 0`) as defined in the catalog. This is recommended by the *GALEX* documentation, as flags could be assigned due to bright star window reflection, dichroic reflection, detector run proximity, or bright star ghost. We exclude targets with measured magnitudes brighter than 15, which marks the saturation limit for both the FUV and NUV photometers (Morrissey et al. 2007).

Based on these thresholds, we find that 462 stars in our sample have NUV photometry and 139 stars have FUV photometry. We explore if flare rate saturation and FUV/NUV saturation are correlated with the derived $R_0$ per star. We present our results in Figure 6. We present the measured FUV/NUV flux normalized by the J-band flux of the star, since it is the fractional flux which acts as an activity indicator. While bolometric lu-
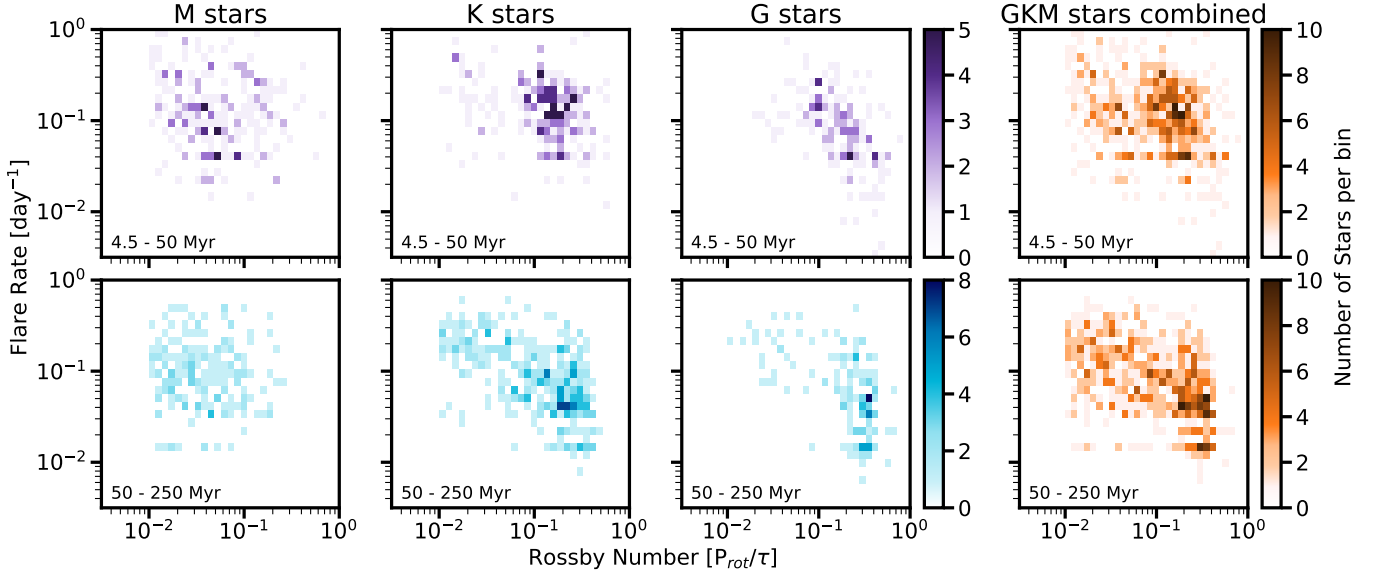
**Figure 5.** Comparison of Rossby Number, $R_0$ and flare rate for young GKM stars. We find no change in the average flare rate for GKM stars $< 250$ Myr. We see evidence that as $R_0$ increases, the average flare rate decreases. This is similar to results presented in Medina et al. (2020), however our sample extends this trend to young GKM stars, while previous results were limited to nearby M dwarfs. The top row are stars with ages $4.5 - 50$ Myr; the bottom row are stars with ages $50 - 250$ Myr. The histograms are colored by number of stars in each bin.

minosities would be a better normalizing factor, we find the majority of stars in our target do not have this parameter measured. To assess FUV/NUV correlations in a larger statistical sense, we thus keep the normalization to $f_J$.

### 4.2. *Comparison to Young Planet Host Stars*

The all-sky observing strategy of TESS has revealed a new population of young transiting exoplanets. Characterizing the local environment for these planets is crucial to understanding their subsequent evolution to forming the mature population of planets. It is debated whether stellar flares are beneficial or detrimental to exoplanets. On one hand, creates life. On the other hand, stellar flares and affiliated coronal mass ejections can permanently alter atmospheric compositions (Chen et al. 2021) and increase the amount of atmospheric mass stripped during the early stages of planet evolution (Feinstein et al. 2020b). To understand the evolution of these new insightful young transiting exoplanets, we compare their measured flare rates to a more statistical sample of stars with similar ages and $T_{\rm eff}$.

We measured the flare rates of planet hosting stars $< 300$ Myr, comparable to the ages of our primary sample. We followed the methods outlined in Section 2 to detect and vet flares. For each star, we created an equivalent sample with respect to both age and $T_{\rm eff}$ to compare the flare rates too. We considered stars with ages $\pm 30$ Myr of the planet hosting star and $T_{\rm eff} \pm 1000$ K. We calculate the flare rate following Equation 3. We present
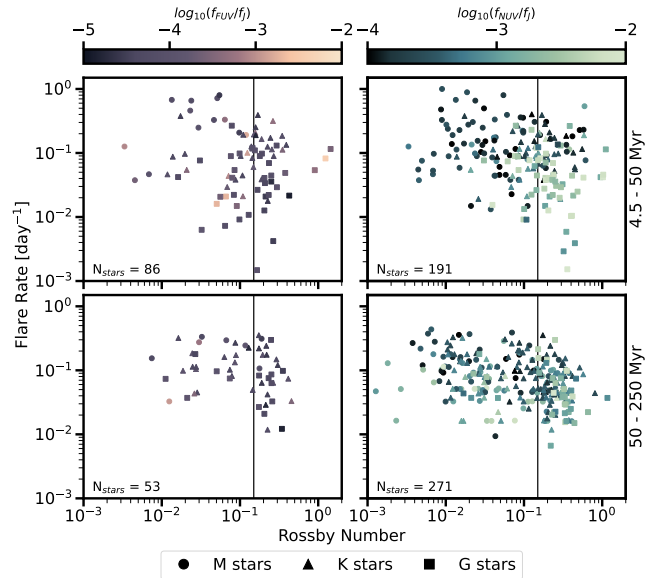


**Figure 6.** Calculated FUV (left) and NUV (right) GALEX flux for stars in our sample. We normalize these values by the J-band flux of the star. We find no strong correlation between the NUV/FUV flux and the measured flare rate or Rossby number. The top row shows GKM stars $< 50$ Myr; the bottom row shows GKM stars $\geq 50$ Myr. M stars are shown as circles, K stars as triangles, and G stars as squares. We note that $f_{NUV}$ traces the photosphere of GK stars, and therefore may not be the best comparison bandpass when looking for trends in magnetic activity.

the flare rates of planet-hosting stars and a comparable

sample of stars in Figure 7 and report the measured rates in Table 2. For the comparable sample, we report the median flare rate, and the lower 16$^{th}$ and upper 84$^{th}$ percentiles.
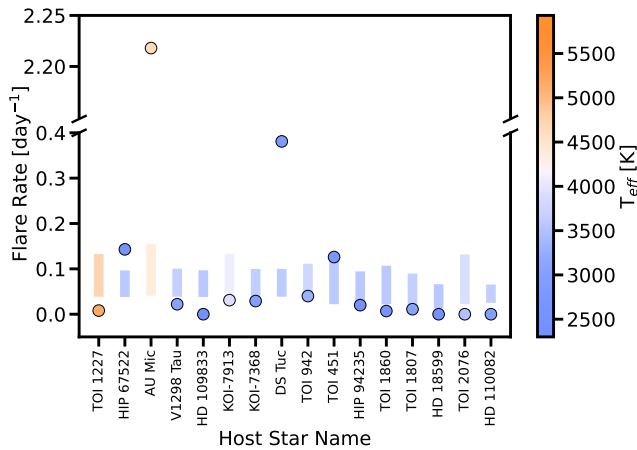


**Figure 7.** Comparison of flare rates from young planet host stars with respect to a comparable sample with respect to age [Myr] and $T_{\rm eff}$ [K]. Circles represent the flare rate of the host star (name along the x-axis); vertical bars represent the lower 16$^{th}$ and upper 84$^{th}$ percentiles for the comparable sample. The majority of young planet hosting stars have flare rates towards the lower end of the comparable sample's distribution. A handful of hosts have more flares, including HIP 67522, AU Mic, DS Tuc A, and TOI 451. We find no correlation between age or $T_{\rm eff}$ that may result in young planet hosts having more or fewer flares than a larger comparable sample. The measured flare rates are presented in Table 2.

### 4.3. *Evidence of Stellar Cycles*

The Sun goes through a 12-year solar cycle, which oscillates between times of high and low activity. The solar cycle manifests itself in a variety of observables, including a change in the flare rate, by a factor of 10 (), and the flare energies released (). Constraints of stellar cycles have predominantly relied on photometry (see recent review by **?**). However, tracing stellar cycles via stellar flares may be more reliable, as flares are a direct consequence of magnetic activity. explored measuring the stellar cycle length of KIC 8507979, a star in the *Kepler* field which was observed for 18 90-day quarters. They found the flare rate decreased over each quarter, which could be fit by $L_{\rm fl}/L_{\rm Kp} = (-9.96 \pm 3.94) \times 10^{-2} \times t_{\rm yr} + (2.43 \pm 0.11)$, where $t_{\rm yr}$ is the time in years, and $L_{\rm fl}/L_{\rm Kp}$ is a parameterization of the *Kepler* flare rate as defined by (Hawley et al. 2014).

It is possible that the length of the stellar cycle is related to the $P_{\rm rot}/R_0$ of the star as ... (). If this is

**Table 2.** Young Planet Host Flare Rates

| Host Name | Age | Flare Rate | Comp. Sample |
|---|---|---|---|
|  | [Myr] | [day$^{-1}$] | Flare Rate [day$^{-1}$] |
| TOI 1227 | $11 \pm 2$ | 0.008 | $0.119^{+0.148}_{-0.046}$ |
| HIP 67522 | $17 \pm 2$ | 0.169 | $0.046^{+0.069}_{-0.020}$ |
| AU Mic | $22 \pm 3$ | 2.218 | $0.133^{+0.171}_{-0.046}$ |
| V1298 Tau | $23 \pm 4$ | 0.022 | $0.074^{+0.091}_{-0.033}$ |
| HD 109833 | $27 \pm 3$ | 0.000 | $0.046^{+0.070}_{-0.020}$ |
| KOI-7913 | $36 \pm 10$ | 0.031 | $0.134^{+0.162}_{-0.045}$ |
| KOI-7368 | $36 \pm 10$ | 0.029 | $0.064^{+0.087}_{-0.030}$ |
| DS Tuc | $45 \pm 4$ | 0.420 | $0.056^{+0.078}_{-0.024}$ |
| TOI 942 | $50^{+30}_{-20}$ | 0.040 | $0.086^{+0.117}_{-0.038}$ |
| TOI 451 | $120 \pm 10$ | 0.128 | $0.071^{+0.085}_{-0.029}$ |
| HIP 94235 | $133^{+15}_{-20}$ | 0.020 | $0.051^{+0.079}_{-0.017}$ |
| TOI 1860 | $133 \pm 26$ | 0.008 | $0.067^{+0.086}_{-0.025}$ |
| TOI 1807 | 18040 | 0.013 | $0.060^{+0.085}_{-0.022}$ |
| HD 18599 | $200^{+200}_{-70}$ | 0.000 | $0.025^{+0.044}_{-0.015}$ |
| TOI 2076 | $204 \pm 50$ | 0.000 | $0.092^{+0.091}_{-0.045}$ |
| HD 110082 | $250^{+50}_{-70}$ | 0.000 | $0.047^{+0.067}_{-0.020}$ |

the case, then stars with $P_{\rm rot}$ will have shorter stellar cycle lengths. The TESS Extended Mission has provided a five-year baseline, similar to *Kepler*, although the sampling is sparser. Within our sample of fast rotators, we searched for evidence of stellar cycles. Our sample contains 31 stars which have been observed for $t_{\rm obs} \geq 400\,{\rm days}$ and $n_{\rm flare} > 100$.

We search for evidence of changes in the stellar magnetic activity by looking at (i) the maximum flare energy in a given period of time and (ii) the flare rate over that same period of time. We grouped our observations by year observed, even if the star was not continuously observed throughout that year.

## 5. CONCLUSIONS

In this work, we present the first measured flare rates for stars $< 300\,{\rm Myr}$ using TESS 2-minute cadence observations. We identified originating 28,822 flares from 3,983 stars. The results of our work are summarized as follows:

1. We measured the flare-frequency distribution (FFD) slope, $\alpha$, for samples of flares binned by age and $T_{\rm eff}$. We find $\alpha$ saturates at $\alpha = -0.5$ for stars younger than 300 Myr and declines after that age. This is the first evidence that, like other tracers of stellar magnetic activity, flare rates saturate across spectral types.

2. We measured the y-intercept, $\beta$, for the same bins of flares. We find that ...

3. We measured the rotation periods, $P_{\rm rot}$ for n stars in our sample using the open-source Python package `michael`.

4. We measured the slope of a truncated power-law, $\alpha_T$, for the same bins of flares. Additionally, we measured $\alpha_T$ as a function of Rossby number, $R_0$.

# APPENDIX

## A. SUPPLEMENTAL MATERIAL

Miscellaneous figures and such that people might want but I don't need to show

## REFERENCES

Bell, C. P. M., Mamajek, E. E., & Naylor, T. 2015, MNRAS, 454, 593, doi: 10.1093/mnras/stv1981

Chang, S. W., Byun, Y. I., & Hartman, J. D. 2015, ApJ, 814, 35, doi: 10.1088/0004-637X/814/1/35

Chen, H., Zhan, Z., Youngblood, A., et al. 2021, Nature Astronomy, 5, 298, doi: 10.1038/s41550-020-01264-1

Curtis, J. L., Agüeros, M. A., Mamajek, E. E., Wright, J. T., & Cummings, J. D. 2019, AJ, 158, 77, doi: 10.3847/1538-3881/ab2899

Davenport, J. R. A., Covey, K. R., Clarke, R. W., et al. 2019, ApJ, 871, 241, doi: 10.3847/1538-4357/aafb76

Davenport, J. R. A., Hawley, S. L., Hebb, L., et al. 2014, ApJ, 797, 122, doi: 10.1088/0004-637X/797/2/122

Feinstein, A., Montet, B., & Ansdell, M. 2020a, The Journal of Open Source Software, 5, 2347, doi: 10.21105/joss.02347

Feinstein, A. D., Montet, B. T., Ansdell, M., et al. 2020b, AJ, 160, 219, doi: 10.3847/1538-3881/abac0a

Feinstein, A. D., Montet, B. T., Foreman-Mackey, D., et al. 2019, PASP, 131, 094502, doi: 10.1088/1538-3873/ab291c

Foreman-Mackey, D., Hogg, D. W., Lang, D., & Goodman, J. 2013, PASP, 125, 306, doi: 10.1086/670067

Gagné, J., Fontaine, G., Simon, A., & Faherty, J. K. 2018, ApJL, 861, L13, doi: 10.3847/2041-8213/aacdff

Galindo-Guil, F. J., Barrado, D., Bouy, H., et al. 2022, A&A, 664, A70, doi: 10.1051/0004-6361/202141114

Gershberg, R. E. 1972, Ap&SS, 19, 75, doi: 10.1007/BF00643168

Goodman, J., & Weare, J. 2010, Communications in Applied Mathematics and Computational Science, 5, 65, doi: 10.2140/camcos.2010.5.65

Günther, M. N., Zhan, Z., Seager, S., et al. 2020, AJ, 159, 60, doi: 10.3847/1538-3881/ab5d3a

Hawley, S. L., Davenport, J. R. A., Kowalski, A. F., et al. 2014, ApJ, 797, 121, doi: 10.1088/0004-637X/797/2/121

Howard, W. S., & MacGregor, M. A. 2022, ApJ, 926, 204, doi: 10.3847/1538-4357/ac426e

Howell, S. B., Sobeck, C., Haas, M., et al. 2014, PASP, 126, 398, doi: 10.1086/676406

Ilin, E., Schmidt, S. J., Davenport, J. R. A., & Strassmeier, K. G. 2019, A&A, 622, A133, doi: 10.1051/0004-6361/201834400

Ilin, E., Schmidt, S. J., Poppenhäger, K., et al. 2021, A&A, 645, A42, doi: 10.1051/0004-6361/202039198

Kerr, R. M. P., Rizzuto, A. C., Kraus, A. L., & Offner, S. S. R. 2021, ApJ, 917, 23, doi: 10.3847/1538-4357/ac0251

Kounkel, M., Covey, K., & Stassun, K. G. 2020, AJ, 160, 279, doi: 10.3847/1538-3881/abc0e6

Luger, R., Bedell, M., Foreman-Mackey, D., et al. 2021, arXiv e-prints, arXiv:2110.06271. https://arxiv.org/abs/2110.06271

Luhman, K. L. 2007, ApJS, 173, 104, doi: 10.1086/520114

Maehara, H., Shibayama, T., Notsu, Y., et al. 2015, Earth, Planets and Space, 67, 59, doi: 10.1186/s40623-015-0217-z

Martin, D. C., Fanson, J., Schiminovich, D., et al. 2005, ApJL, 619, L1, doi: 10.1086/426387

Medina, A. A., Winters, J. G., Irwin, J. M., & Charbonneau, D. 2020, ApJ, 905, 107, doi: 10.3847/1538-4357/abc686

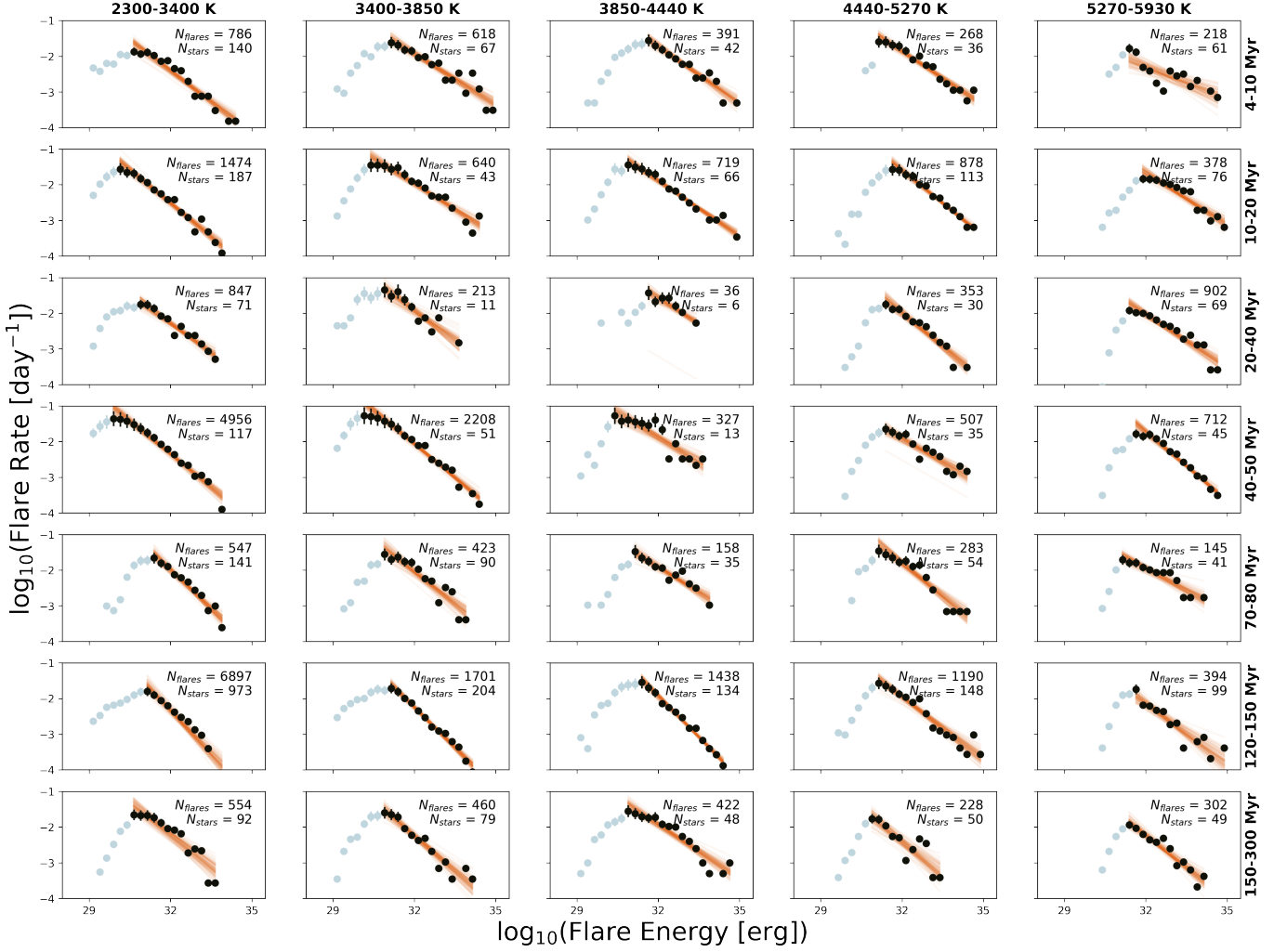Morrissey, P., Conrow, T., Barlow, T. A., et al. 2007, ApJS, 173, 682, doi: 10.1086/520512

**Figure A1.** Flare frequency distributions (FFDs) for subgroups of stars, clustered by age and effective temperature, $T_{\rm eff}$. Flares were binned into 25 bins in log-space from $10^{27} - 10^{35}$ erg. We fit the FFD from the turn-over in the binned flares, likely a result of very low-energy flares being missed in our flare-detection algorithm. The bins used to fit the FFD are shown in black, while all bins are shown in gray. We ran an MCMC fit to these distributions with a simple power law; 100 random samples from these fits are over-plotted in orange. We fit distributions with $> 3$ bins. The best-fit slopes from these fits are presented in Figure 3.

Murphy, S. J., & Lawson, W. A. 2015, MNRAS, 447, 1267, doi: 10.1093/mnras/stu2450

Notsu, Y., Shibayama, T., Maehara, H., et al. 2013, ApJ, 771, 127, doi: 10.1088/0004-637X/771/2/127

Okamoto, S., Notsu, Y., Maehara, H., et al. 2021, ApJ, 906, 72, doi: 10.3847/1538-4357/abc8f5

Pecaut, M. J., & Mamajek, E. E. 2016, MNRAS, 461, 794, doi: 10.1093/mnras/stw1300

Pizzolato, N., Maggio, A., Micela, G., Sciortino, S., & Ventura, P. 2003, A&A, 397, 147, doi: 10.1051/0004-6361:20021560

Ricker, G. R., Winn, J. N., Vanderspek, R., et al. 2015, Journal of Astronomical Telescopes, Instruments, and Systems, 1, 014003, doi: 10.1117/1.JATIS.1.1.014003

Röser, S., Schilbach, E., & Goldman, B. 2016, A&A, 595, A22, doi: 10.1051/0004-6361/201629158

Schneider, A. C., & Shkolnik, E. L. 2018, AJ, 155, 122, doi: 10.3847/1538-3881/aaaa24

Seligman, D. Z., Rogers, L. A., Feinstein, A. D., et al. 2022, ApJ, 929, 54, doi: 10.3847/1538-4357/ac5b69

Shibayama, T., Maehara, H., Notsu, S., et al. 2013, ApJS, 209, 5, doi: 10.1088/0067-0049/209/1/5

Silverberg, S. M., Kowalski, A. F., Davenport, J. R. A., et al. 2016, ApJ, 829, 129, doi: 10.3847/0004-637X/829/2/129

Tarricq, Y., Soubiran, C., Casamiquela, L., et al. 2021, A&A, 647, A19, doi: 10.1051/0004-6361/202039388

Tofflemire, B. M., Rizzuto, A. C., Newton, E. R., et al. 2021, AJ, 161, 171, doi: 10.3847/1538-3881/abdf53

Tovar Mendoza, G., Davenport, J. R. A., Agol, E., Jackman, J. A. G., & Hawley, S. L. 2022, AJ, 164, 17, doi: 10.3847/1538-3881/ac6fe6

Wright, N. J., Drake, J. J., Mamajek, E. E., & Henry, G. W. 2011, ApJ, 743, 48, doi: 10.1088/0004-637X/743/1/48

Wright, N. J., Newton, E. R., Williams, P. K. G., Drake, J. J., & Yadav, R. K. 2018, MNRAS, 479, 2351, doi: 10.1093/mnras/sty1670